Inorganic Chemistry

Article

pubs.acs.org/IC

Role of Bond Strength on the Lattice Thermal Expansion and Oxide Ion Conductivity in Quaternary Pyrochlore Solid Solutions

A. N. Radhakrishnan,[†] P. Prabhakar Rao,*[,†] S. K. Mahesh,[†] D. S. Vaisakhan Thampi,[†] and Peter Koshy[‡]

[†]Materials and Minerals Division, National Institute for Interdisciplinary Science and Technology (NIIST), Trivandrum 695 019, India

[‡]Mount Zion College of Engineering for Women, Chengannur 689 521, India

ABSTRACT: Quaternary pyrochlore-type solid solutions, $CaGdZrNb_{1-x}Ta_xO_7$ (x = 0, 0.2, 0.4, 0.6, 0.8, 1), were prepared by a high-temperature ceramic route. The pyrochlore phases of the compounds were confirmed by powder X-ray diffraction (XRD), Raman spectroscopy, and transmission electron microscopy. The crystallographic parameters of the pyrochlore compounds were accurately determined by Rietveld analysis of the powder XRD data. The isovalent substitution of Ta in place of Nb at the B site can reveal the effect of chemical bonding on lattice thermal expansion and oxide ion conductivity because both Nb and Ta have the same ionic radius (0.64 Å). Lattice thermal expansion coefficients of the samples were calculated from high-temperature XRD measurements, and it was found that the thermal expansion coefficient decreases with substitution of Ta. Oxide ion conductivity measured by a two-probe method also shows the same trend with substitution of Ta, and this can be attributed to the high bond strength of the Ta−O bond compared to that of the Nb−O bond. Microstructural characterization using scanning electron microscopy proves that the size of the grains has a small effect on the oxide ion conductivity. Our studies established the role of chemical bonding in deciding the conductivity of pyrochlore oxides and confirmed that the 48f−48f mechanism of oxide ion conduction is dominant in pyrochlore oxides.

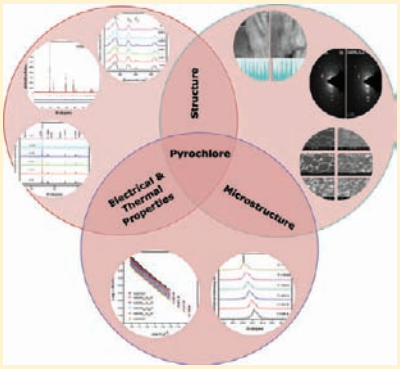

1. INTRODUCTION

Oxides with the pyrochlore structure have been the subject of a number of investigations in the last few decades and exhibit diverse properties such as semiconductivity,[1,2] ionic conductivity,[3,4] superconductivity,[5,6] high radiation tolerance,[7] dielectric properties,[8] and luminescence properties.[9] Pyrochlore oxides have the general formula $A_2B_2O_7$, where A is the larger cation and B is the smaller one. Mostly, A is a trivalent rare-earth ion but can also be a mono- or divalent cation, and B may be a 3d, 4d, or 5d transition element having an appropriate oxidation state required for charge balance to give rise to the composition $A_2B_2O_7$. Pyrochlore oxides lend themselves to a wide variety of chemical substitutions at the A, B, and O sites, and the crystal structure can tolerate vacancies at the A and O sites to a certain extent. This structure is closely related to fluorite and can be considered as an ordered, defect fluorite-structured material with anion vacancies.[10,11] Owing to their unique structural characteristics, pyrochlore oxides show high chemical stability, high catalytic activity, high melting temperature, and excellent oxide ion conductivity. Oxide-ion-conducting pyrochlores find applications in solid oxide fuel cells (SOFCs) as electrolytes[12] and gas sensors.[13]

Generally, pyrochlores are of two major classes depending upon the combination of oxidation states, namely, (2+, 5+) pyrochlores and (3+, 4+) pyrochlores. The pyrochlore structure has only one parameter; the 48f O x value needs to be defined in the structure containing four different kinds of atoms: A (16d), B (16c), O (48f), and O′ (8b). However, the 8- and 6-fold-coordination polyhedra of oxygen around the A and B cations, respectively, in $A_2B_2O_7$ change shape with x, and the entire structure can be viewed in several different ways. A comprehensive account of the crystal structure, field of stability, synthesis, and physical properties of $A_2^{3+}B_2^{4+}O_7$ (3+, 4+), $A_2^{2+}B_2^{5+}O_7$ (2+, 5+), and various substituted pyrochlores is presented in a review by Subramanian et al.[14] Many of the pyrochlore oxides known in the literature are of the (3+, 4+) type and are due to the fact that a large number of A^{3+} and B^{4+} cations have suitable ionic radii for formation of the pyrochlore structure. The relative ionic radii or the ionic radius ratio (RR = r_A/r_B) and the oxygen parameter govern the formation and stability of the (3+, 4+) type oxide pyrochlores. A relatively fewer number of (2+, 5+) oxide pyrochlores are known in comparison to the large number of available (3+, 4+) pyrochlores. This is because there are fewer suitable A^{2+} and B^{5+} cations than A^{3+} and B^{4+} cations. It is not possible to define the field of existence in terms of RR more accurately because of the absence of elements of closely related ionic radii similar to the rare earths in the (3+, 4+) pyrochlores. However, the (2+, 5+) pyrochlores are unique in that the covalency, polarizability, and electronegativity of the constituent ions give rise to a wide variety of interesting physical properties.[14]

Received: November 3, 2011
Published: January 26, 2012

   dx.doi.org/10.1021/ic202383f | *Inorg. Chem.* 2012, 51, 2409−2419

Quaternary pyrochlore systems with the general formula $A_1^{2+}A_2^{3+}B_1^{4+}B_2^{5+}O_7$ can be considered as a combination of two types of pyrochlores. However, detailed phase diagram studies[15] established that the quaternary phases crystallizing with the cubic pyrochlore structure are indeed well-defined stoichiometric phases and not solid solutions of two binary phases. The presence of multivalent cations can induce distortions in the structure, which, in turn, affects the thermal and electrical properties of the compounds. Structure−property correlation studies provide a basic understanding required for the design of new oxide ion conductors, which can be used in intermediate-temperature SOFCs as electrolytes. Researches in the field of SOFCs have recently gained more attention because of great concerns over the energy crisis and environmental pollution. Kutty et al.[16] reported a systematic study of the thermal expansion coefficients of lanthanide pyrochlore zirconates and hafnates and found that the thermal expansion coefficient decreases with an increase in the A cation radius. They have correlated thermal expansion behavior with the oxygen x parameter, Madelung binding energy, and finally bond strength. An extensive amount of experimental data on the relationship between oxide ion conductivity and structural disorder are available in the literature,[17] mostly in (3+, 4+) pyrochlore oxides with substitutions at either the A site[18] or B site.[19] We have recently reported the influence of disorder on the structure, lattice thermal expansion, and oxide ion conducting properties of $(Ca_xGd_{1-x})_2(Zr_{1-x}M_x)_2O_7$ (M = Nb, Ta) pyrochlore solid solutions.[20] Disorder in pyrochlore can enhance oxide ion conductivity but also led to high thermal expansion of the lattice. The influence of chemical bonding on lattice thermal expansion and oxide ion conductivity was not investigated in quaternary pyrochlores, and such an investigation enables one now to predict the ionic conductivity based on the elemental composition of a particular compound, which is important in materials design for SOFC applications. In the present study, $CaGdZrNb_{1-x}Ta_xO_7$ (x = 0, 0.2, 0.4, 0.6, 0.8, 1) was prepared and characterized to establish the correlation among the structure, lattice thermal expansion, and oxide ion conductivity. The study is particularly focused on relating the bond strength to lattice thermal expansion and oxide ion conductivity so that one can predict unambiguously lattice expansion and oxide ion conductivity from the bond strengths.

2. EXPERIMENTAL SECTION

$CaGdZrNb_{1-x}Ta_xO_7$ (x = 0, 0.2, 0.4, 0.6, 0.8, 1) samples were prepared by the conventional ceramic route using the starting materials $CaCO_3$, Gd_2O_3, ZrO_2, Nb_2O_5, and Ta_2O_5 (Sigma-Aldrich, 99.99%). The raw materials were weighed according to the stoichiometry of the samples and then mixed thoroughly in an agate mortar. Acetone was added to the powdered mixture for proper mixing. Then, the mixture was dried in an air oven at 100 °C for 1 h. This procedure of mixing and subsequent drying was repeated three times to get a homogeneous mixture. The powdered samples were calcined at 1300 °C for 6 h, followed by a second calcination at 1400 °C for 10 h.

The calcined product was ground into a fine powder and then mixed with a 2 wt % solution of poly(vinyl alcohol) as the organic binder for strengthening and good compaction of the pellet. The dried powder was pressed into cylindrical pellets of 10 mm diameter and about 2−3 mm thickness using a hydraulic press. Pellets were initially heated to 600 °C, kept for 30 min to completely remove the organic binder, and sintered for 36 h at 1550 °C to optimize the density of the samples (density data are given in Table 1). Powder X-ray diffraction (XRD) patterns were recorded to identify the crystalline phase of the sintered samples using Ni-filtered Cu Kα radiation by a Philips X'pert diffractometer (step size = 0.02, scanning time per step = 20 s, divergence slit = 0.5, and exported by *X'pert Pro* software). The unit cell parameters were calculated by a least-squares method, and Rietveld analysis was also performed to refine the structure using *Fullprof-2010*. For lattice thermal expansion studies, the XRD pattern of the sample was recorded from 2θ = 10 to 90°, in the temperature range 293−1273 K on a Philips X'pert Pro XRD unit equipped with an Anton Paar HTK attachment, at a regular interval of 200 K, in static air. The Fourier transform (FT) near-IR (NIR) Raman spectra of the powdered samples were recorded on a Bruker RFS100/S spectrometer using NIR laser excitation (Nd:YAG, 1064 nm). A standard Ge detector cooled to liquid-nitrogen temperature was used, and it was set to scan over the range from 50 to 1000 cm^{-1}. The resolution of the spectrometer is 4 cm^{-1}. The selected-area electron diffraction (SAED) patterns and high-resolution electron microscopy of the samples were taken using a TECNAI 30G2 S-TWIN transmission electron microscope (FEI, The Netherlands). A small amount of finely powdered sample is dispersed in an acetone medium by ultrasonication, drop-casted onto carbon-coated copper grids, and dried. The sintered pellets were polished and thermally etched near the sintering temperature for about 30 min. The grain microstructure on the surface of the thermally etched samples was recorded using a scanning electron microscope (JEOL, JSM 5600 LV). For impedance spectroscopic studies, a high-temperature-curing silver paste was applied on polished flat faces of the pellet and electroded with long silver wires. The electroded pellets were cured in a tube furnace for 0.5 h at 600 °C. Impedance measurements of the pellets were carried out from 400 to 750 °C in the frequency range 10 Hz to 1 MHz using a computer-controlled impedance analyzer (Solartron, SI 1260). The complex impedance plots were made with *SMART* software supplied by M/s Solartron (Schlumberger, U.K.).

Table 1. Theoretical, Experimental, and Relative Densities of $CaGdZrNb_{1-x}Ta_xO_7$ (x = 0, 0.2, 0.4, 0.6, 0.8, 1) Samples Sintered at 1550 °C for 36 h

compound	theoretical density (g/cm^3)	experimental density (g/cm^3)	relative density (%)
$CaGdZrNbO_7$	5.6384	5.4388	96.46
$CaGdZrNb_{0.8}Ta_{0.2}O_7$	5.8313	5.6109	96.22
$CaGdZrNb_{0.6}Ta_{0.4}O_7$	6.0424	5.8019	96.02
$CaGdZrNb_{0.4}Ta_{0.6}O_7$	6.2430	5.9758	95.72
$CaGdZrNb_{0.2}Ta_{0.8}O_7$	6.4463	6.1653	95.64
$CaGdZrTaO_7$	6.6484	6.3532	95.56

3. RESULTS AND DISCUSSION

3.1. Powder XRD Studies. Powder XRD patterns of $CaGdZrNb_{1-x}Ta_xO_7$ (x = 0, 0.2, 0.4, 0.6, 0.8, 1) samples sintered at 1550 °C are shown in Figure 1. Patterns can be well-indexed with an ideal cubic pyrochlore structure belonging to the $Fd\bar{3}m$ space group. Pyrochlore is a superstructure of a fluorite-type unit cell, which has a typical face-centered-cubic arrangement of cations with anions in the tetrahedral holes. The pyrochlore unit cell also has similar arrangements except for the fact that there are two different kinds of cations and, consequently, two crystallographically nonequivalent anion sites (48f and 8b) and an anion vacancy (8a). Hence, the XRD pattern of a typical pyrochlore consists of a set of strong intensities representing an average fluorite structure plus an additional set of superstructure intensities. The diffraction peaks corresponding to an average fluorite structure in the pyrochlore satisfy the set of conditions[21]

$$h + k = 4n$$
$$k + l = 4n$$
$$h + l = 4n \quad (1)$$

dx.doi.org/10.1021/ic202383f | *Inorg. Chem.* 2012, 51, 2409−2419

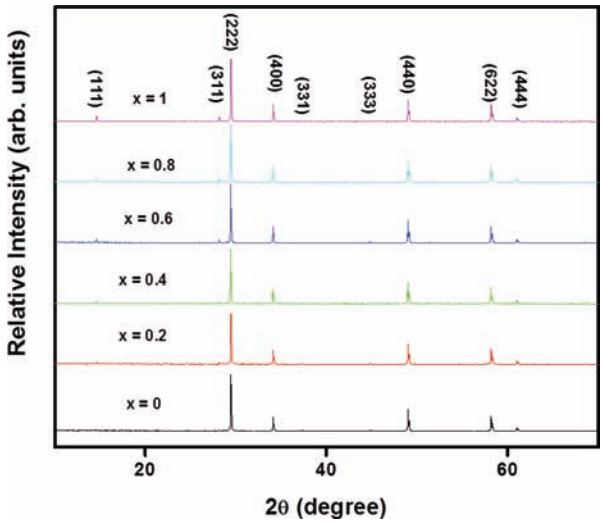

Figure 1. Powder XRD patterns of $CaGdZrNb_{1-x}Ta_xO_7$ (x = 0, 0.2, 0.4, 0.6, 0.8, 1) samples sintered at 1550 °C. Patterns can be well-indexed with an ideal cubic pyrochlore structure belonging to the $Fd\bar{3}m$ space group. XRD pattern of a typical pyrochlore consists of a set of strong intensities representing an average fluorite structure plus an additional set of superstructure intensities. Superlattice peaks in the diffraction pattern corresponding to peaks with odd Miller indices like (111), (311), etc.

where (hkl) are the Miller indices of the plane and n is an integer. These peaks have a large contribution from the cation sublattice because of the high scattering power of the electron-rich rare-earth elements and transition metals compared to that of O atoms. Superlattice peaks in the diffraction pattern do not satisfy the conditions (1), and Miller indices (hkl) corresponding to these peaks are all odd. The superstructure intensities depend on the difference in the scattering power between the A and B cations, distortion of the anion array, distribution of oxygen vacancies, and oxygen x parameter.[21] Superlattice peaks are observed to be less intense for $CaGdZrNbO_7$, and as the doping level of Ta increases, the superlattice peaks like (111) and (311) become more intense. This can be attributed to the fact that the presence of Ta leads to more ordering in the structure and reduces the distortion of the anion sublattice. This variation in the intensity of the superlattice peaks can also be due to the high X-ray scattering power of Ta compared to that of Nb.

Rietveld analysis of the powder XRD patterns was performed using *Fullprof-2010* software in order to quantify the structural changes within the unit cell due to the progressive substitution of Ta in place of Nb. The initial structure model was based on an ideal pyrochlore structure with the $Fd\bar{3}m$ space group, and occupancies are decided as per the stoichiometry of the compositions. First of all, the scale factor and background parameters were fitted. The diffraction peak profile was fitted with a pseudo-Voigt profile function, and Caglioti profile parameters were refined. Absorption and extinction coefficients were not considered during refinement. The lattice parameter and oxygen x parameter were refined for all samples. Two typical XRD patterns after Rietveld refinement are given in Figure 2, and the results of refinement are given in Table 2. From Rietveld analysis, it was found that substitution of Ta in place of Nb leads to a slight decrease in the lattice parameter, as is evident from the composition versus lattice parameter graph shown in Figure 3, along with the composition versus oxygen x parameter graph. Variation of the oxygen x parameter also follows the same trend as that of the lattice parameter. This is an interesting observation of lattice contraction with substitution of Ta even though the ionic radii of Nb and Ta are the same (0.64 Å) when six-coordinated. The decrease in the lattice parameter with substitution of Ta may be due to the fact that the nuclear charge of Ta is high compared to that of Nb, which attracts the electron cloud around it, making the bond shorter. This makes the bond stronger and causes the unit cell to shrink a little.

3.2. Raman Spectroscopic Studies. Cubic pyrochlores, $A_2B_2O(1)_6O(2)$, belong to the space group $Fd\bar{3}m$ (No. 227), where Z = 8. The number of molecular units per primitive unit cell is 2. The corresponding factor group for the cubic pyrochlore is O_h. The site symmetry is D_{3d} for the A and B cations, C_{2v} for the O(1) anion, and T_d for the O(2) anion.[22] Factor group analysis based on the above assumptions predicted 26 vibrational normal modes, out of which only 6 are Raman-active.[23] The irreducible representations of the 6 Raman-active modes are given as follows:

$$\Gamma(\text{Raman}) = A_{1g} + E_g + 4F_{2g} \quad (2)$$

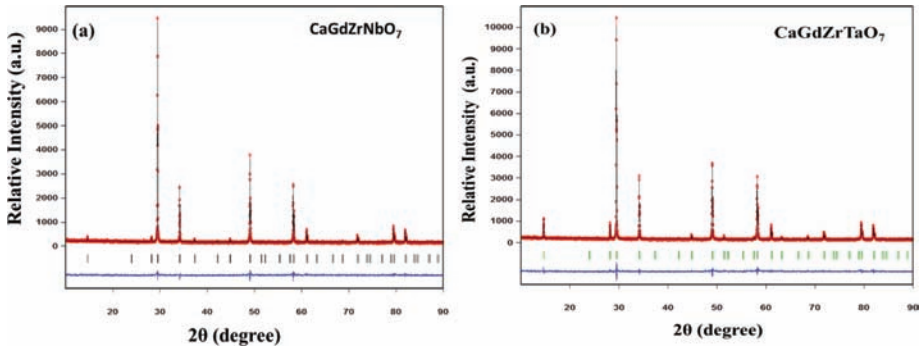

Figure 2. Observed, calculated, and difference XRD profiles of (a) $CaGdZrNbO_7$ and (b) $CaGdZrTaO_7$ after Rietveld refinement. Rietveld analysis of the powder XRD patterns was performed using *Fullprof-2010* software, the initial structure model was based on an ideal pyrochlore structure with the $Fd\bar{3}m$ space group, and occupancies are decided as per the stoichiometry of the compositions. First of all, the scale factor and background parameters were fitted. The diffraction peak profile was fitted with a pseudo-Voigt profile function, and Caglioti profile parameters were refined. Absorption and extinction coefficients were not considered during refinement. The lattice parameter and oxygen x parameter were refined for all samples.

dx.doi.org/10.1021/ic202383f | *Inorg. Chem.* 2012, 51, 2409–2419

Table 2. Rietveld Refined Parameters of $CaGdZrNb_{1-x}Ta_x O_7$ (x = 0, 0.2, 0.4, 0.6, 0.8, 1) Samples

sample		x = 0	x = 0.2	x = 0.4	x = 0.6	x = 0.8	x = 1
phase		pyrochlore	pyrochlore	pyrochlore	pyrochlore	pyrochlore	pyrochlore
unit cell		cubic	cubic	cubic	cubic	cubic	cubic
space group		$Fd\bar{3}m$	$Fd\bar{3}m$	$Fd\bar{3}m$	$Fd\bar{3}m$	$Fd\bar{3}m$	$Fd\bar{3}m$
total no. of indep reflns		43	43	43	43	43	43
lattice constant (Å)		10.5139(6)	10.5134(7)	10.5130(2)	10.5125(6)	10.5122(2)	10.5118(5)
fwhm	U	0.0111(6)	0.0192(8)	0.0215(1)	0.0198(1)	0.0256(8)	0.0265(2)
parameters	V	−0.0042(1)	−0.0103(2)	−0.0110(3)	−0.0092(5)	−0.0113(4)	−0.0116(8)
	W	0.0012(1)	0.00253(3)	0.0022(7)	0.0021(5)	0.0026(5)	0.0027(2)
zero		0.0421(1)	0.0495(3)	0.0080(2)	0.0256(8)	0.0266(7)	0.0485(8)
asymmetry		−0.0015(7)	0.0319(1)	0.0292(7)	0.0292(8)	0.0453(9)	0.0606(2)
parameters		0.0162(3)	0.0022(4)	−0.0033(5)	0.0077(5)	0.0080(2)	0.0137(4)
oxygen x parameter		0.3291(1)	0.3286(2)	0.3281(6)	0.3276(6)	0.3270(5)	0.3265(3)
overall B factor		0.2021(7)	0.1498(2)	0.2656(7)	0.1650(3)	0.1859(5)	0.2234(5)
R factors	R_p	6.74	6.84	6.60	6.61	6.38	6.52
	R_{wp}	8.64	8.76	8.51	8.51	8.22	8.38
	R_{exp}	6.85	6.98	6.96	6.87	6.77	6.78
	χ^2	1.59	1.58	1.50	1.54	1.47	1.53
	GOF	1.3	1.3	1.2	1.2	1.2	1.2

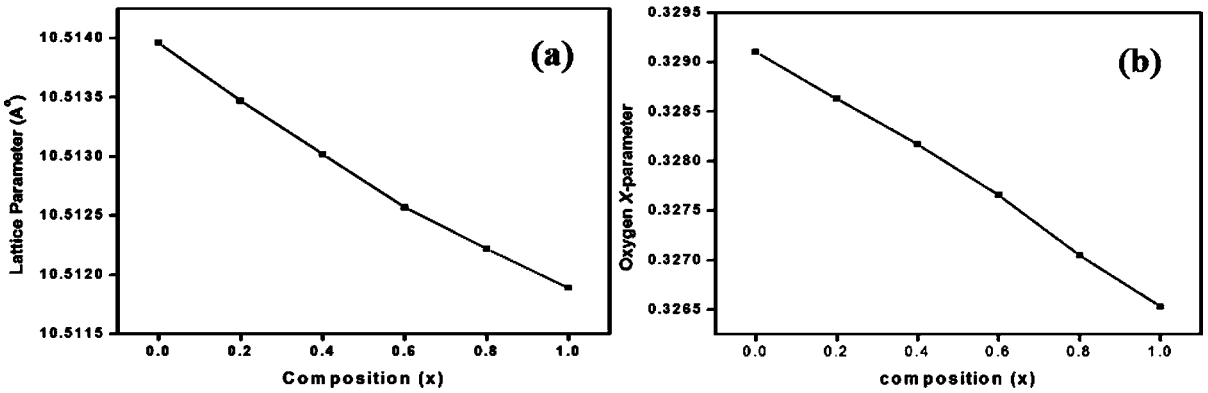

Figure 3. Variation of (a) lattice parameter and (b) oxygen x parameter with composition. The lattice parameter as well as oxygen x parameter decreases with substitution of Ta in place of Nb, even if the ionic radii of Nb and Ta are the same (0.64 Å) when six-coordinated. The decrease in the lattice parameter with substitution of Ta may be due to the fact that the nuclear charge of Ta is high compared to that of Nb, which attracts the electron cloud around it, making the bond shorter. This makes the bond stronger and causes the unit cell to shrink a little.

Figure 4 shows the FT Raman spectra of $CaGdZrNb_{1-x}Ta_xO_7$ (x = 0, 0.2, 0.4, 0.6, 0.8, 1) samples sintered at 1550 °C. Only three modes having high intensity are marked in the figure as other modes are very weak in intensity, and these modes can be assigned to vibrations of BO_6 octahedra in accordance with Vandenborres and co-workers' work on pyrochlores.[24] The E_g mode appearing around ∼350 cm^{-1} is the most prominent mode of the pyrochlore and appears to be very broad because of the presence of two different cations at the B site. This broadening is not due to smaller particle size because the samples are prepared by a solid-state high-temperature route and the XRD patterns are reasonably sharp, which confirms the fact that the sizes of the particles are in the microregime. The A_{1g} mode appearing around ∼545 cm^{-1} can be assigned to O−B−O bending. Both E_g and A_{1g} do not have any change in intensity with respect to Ta doping. The four F_{2g} modes of the pyrochlore are usually observed around 300, 400, 510, and 610 cm^{-1}.[25] The absence of F_{2g} modes around 300 and 510 cm^{-1} in the Raman spectra is due to the overlap produced by broadening of the E_g and A_{1g} modes. The F_{2g} mode appearing around 400 cm^{-1} is very weak in intensity, and according to group factor analysis, the 8b site oxygen is related to this mode.[26] F_{2g} appearing around ∼600 cm^{-1} has considerable intensity, and the intensity decreases steadily with Ta substitution for Nb. This mode is linked with 48f O,[27] and a decrease in intensity with Ta doping may be due to the restricted vibration of the B−O bond due to high bond strength and subsequent shrinkage of BO_6 induced by Ta doping. This is evident from the decrease in the oxygen x parameter with doping, as shown in Figure 3b and its explanation in the text. The mode appearing around 830 cm^{-1} is reported in the literature as a combination band and arises because of distortion of BO_6 octahedra and subsequent relaxation of the selection rules.[28] The intensity of this mode is also found to decrease with an increase in Ta doping, and this may be due to the fact that Ta substitution reduces the symmetry distortion of the BO_6 octahedra. These effects are not due to the ionic-size-induced distortion but the change in the shape of the octahedra induced by chemical bonding.

dx.doi.org/10.1021/ic202383f | Inorg. Chem. 2012, 51, 2409−2419

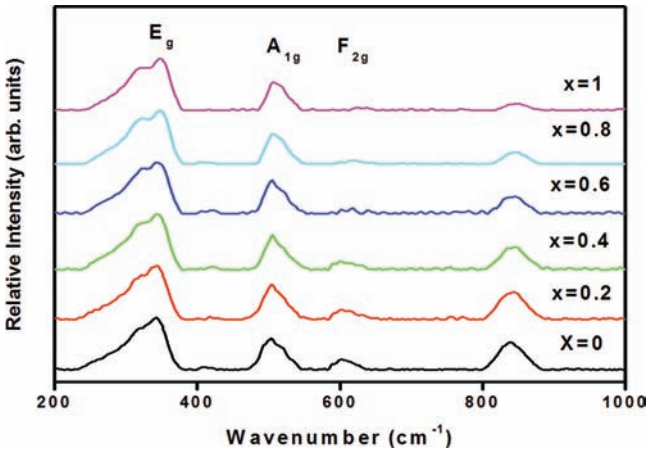

Figure 4. FT Raman spectra of $CaGdZrNb_{1-x}Ta_xO_7$ (x = 0, 0.2, 0.4, 0.6, 0.8, 1) samples. On the basis of factor group analysis of the cubic pyrochlore structure belonging to the $Fd\bar{3}m$ (No. 227) space group, there are only six Raman-active modes represented as $\Gamma(\text{Raman}) = A_{1g} + E_g + 4F_{2g}$, out of which three modes are marked in the figure and the other three modes are very weak in intensity and are not visible in the spectra. The mode appearing around 830 cm^{-1} is reported in the literature as a combination band and arises because of distortion of the BO_6 octahedra and subsequent relaxation of the selection rules.

3.3. Transmission Electron Microscopy (TEM) Studies. TEM is the best tool to explore the structures of the compounds at their atomic levels. Figure 5 shows the high-resolution images of the two representative samples along with histograms of a few lattice planes. Pyrochlore superlattice plane (111) is observed in both cases, and the corresponding lattice spacing is marked in the figure, which corroborates the XRD results. Histograms of the planes show the presence of an intermediate plane of atoms between the (111) plane approximately at a half distance between them. This plane is (222) with exactly half the lattice spacing, and it is the most intense plane in the XRD pattern. Figure 6 shows the SAED patterns of two samples. Major planes of the pyrochlores were indexed using the ratio method, and they are compared with the corresponding XRD profiles. Superlattice planes of the pyrochlores appear only as a few scattered spots instead of rings, which is typical of polycrystalline materials. The (111) plane is merged into the high-intensity transmitted beam at the center.

3.4. High-Temperature XRD Studies. For high-temperature applications of functional materials, the structural stability with temperature is a key factor to be investigated. The lattice thermal expansion coefficient is the best estimate of the structural stability with temperature and can be easily determined

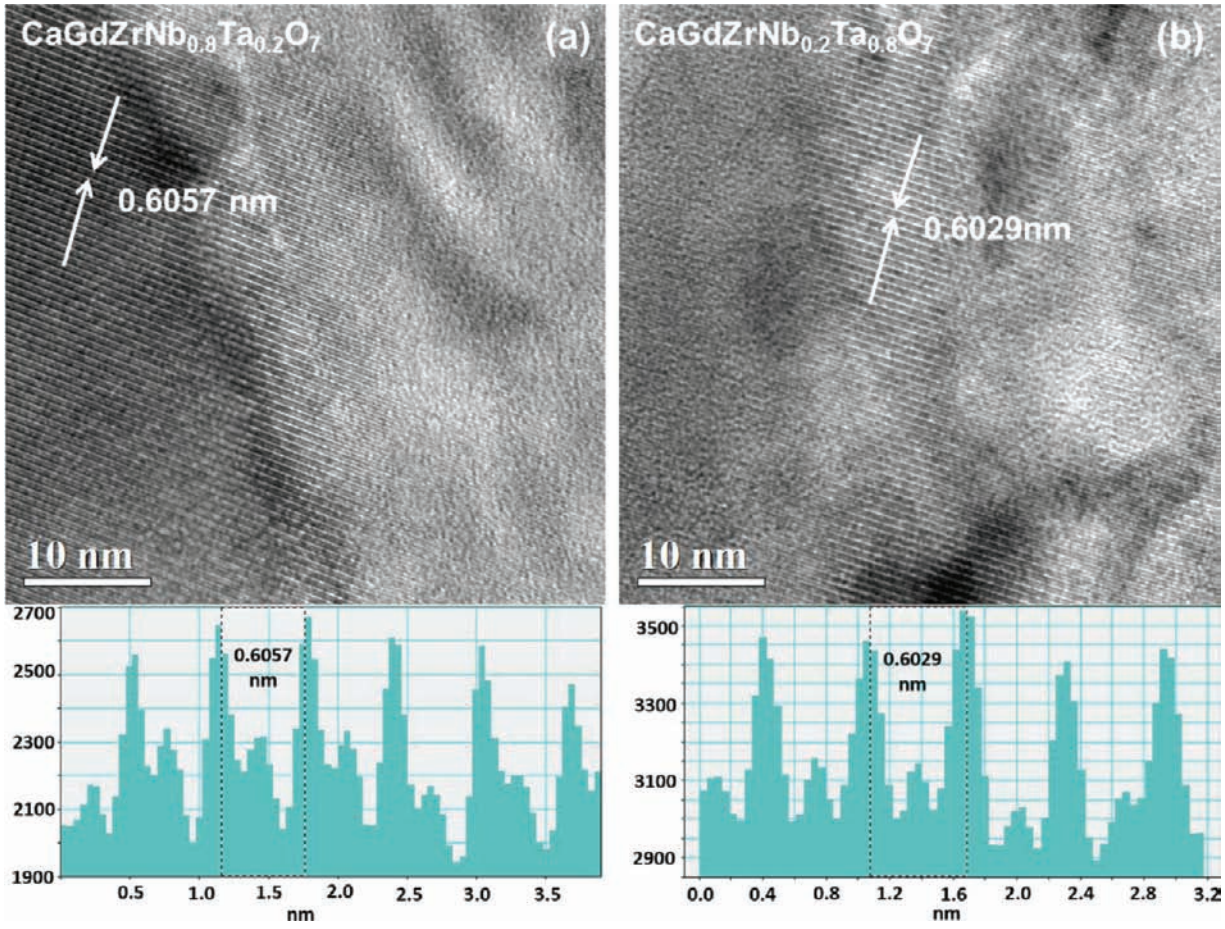

Figure 5. High-resolution images and the corresponding histogram profiles of a few lattice planes of (a) $CaGdZrNb_{0.8}Ta_{0.2}O_7$ and (b) $CaGdZrNb_{0.2}Ta_{0.8}O_7$ samples. Pyrochlore superlattice plane (111) is observed in both cases, and the corresponding lattice spacing is marked in the figure, which corroborates the XRD results. Histograms of the planes show the presence of an intermediate plane of atoms between the (111) plane approximately at a half distance between them. This plane is (222) with exactly half the lattice spacing, and it is the most intense plane in the XRD pattern.

dx.doi.org/10.1021/ic202383f | Inorg. Chem. 2012, 51, 2409–2419

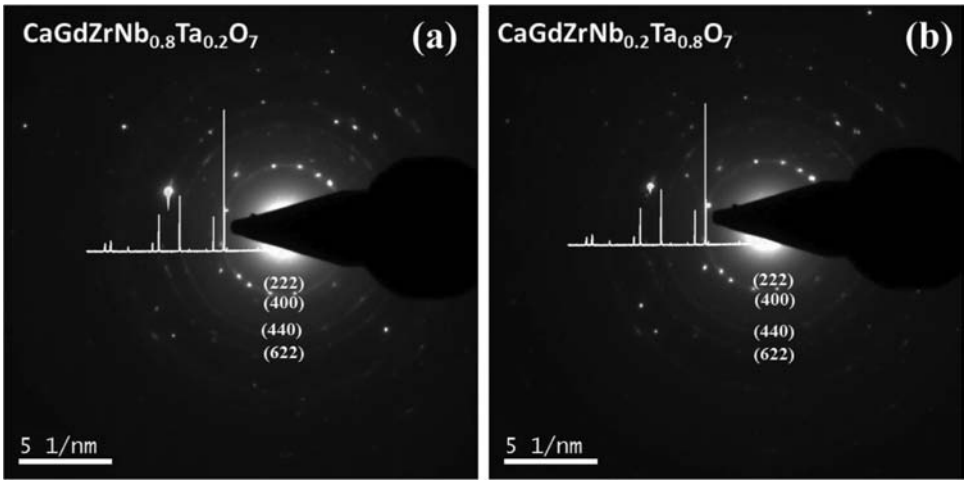

Figure 6. SAED patterns of (a) $CaGdZrNb_{0.8}Ta_{0.2}O_7$ and (b) $CaGdZrNb_{0.2}Ta_{0.8}O_7$ samples. Major planes of the pyrochlores were indexed using the ratio method, and they are compared with the corresponding XRD profiles. Superlattice planes of the pyrochlores appear only as a few scattered spots instead of rings, which is typical of polycrystalline materials. The (111) plane is merged into the high-intensity transmitted beam at the center.

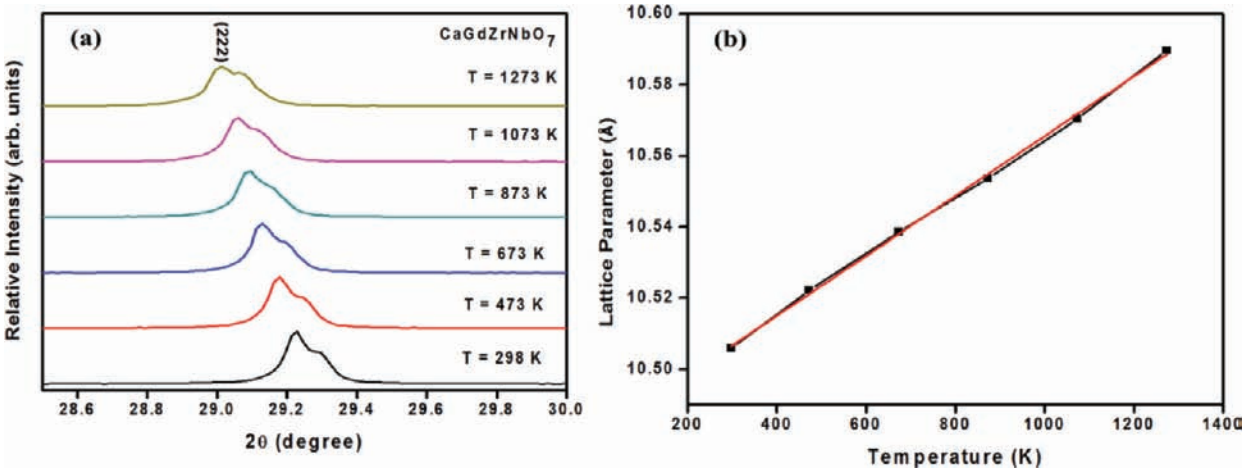

Figure 7. (a) High-temperature XRD patterns of $CaGdZrNbO_7$ at different temperatures and (b) the corresponding lattice parameter versus temperature plot. The XRD patterns were recorded for each sample at different temperatures and fitted by the Lebail fitting method using X'pert High Score Plus software. For each sample, plots were made with the lattice parameter as a function of the absolute temperature. The slope of the graph (da/dT) was calculated by a linear fit of the graph, and the lattice thermal expansion coefficient was calculated using the equation $\alpha_a = (1/a_{298})(da/dT)$ K^{-1}.

using high-temperature XRD. The lattice thermal expansion coefficient is calculated using the equation

$$\alpha_a = \frac{1}{a_{298}}\left(\frac{da}{dT}\right) \quad K^{-1} \tag{3}$$

The XRD patterns were recorded for each sample at different temperatures and fitted by the Lebail fitting method using X'pert High Score Plus software. For each sample, plots were made with the lattice parameter as a function of the absolute temperature. The slope of the graph (da/dT) was calculated by a linear fit of the graph, and the lattice thermal expansion coefficient was calculated using the above equation. High-temperature XRD patterns of $CaGdZrNbO_7$ at different temperatures and the corresponding lattice parameter versus temperature plots are shown in Figure 7. In the high-temperature XRD pattern, only the (222) peak is shown and the shift of the peak to the lower angle as the temperature increases indicates expansion of the lattice.

Variation of the lattice thermal expansion coefficient with different compositions, $CaGdZrNb_{1-x}Ta_xO_7$ (x = 0, 0.2, 0.4, 0.6, 0.8, 1), is shown in Figure 8. In pyrochlore-type compositions, the thermal expansion coefficient decreases with an increase in the substitution of Ta. Thermal expansion of zirconate pyrochlores depends on the Madelung binding energy, and as Madelung binding energy increases, thermal expansion decreases.[29] The Madelung binding energy of zirconate pyrochlores depends on the 48f O x parameter, and as the x parameter decreases, the Madelung energy increases.[14] The experimental results of our high-temperature XRD studies were in good agreement with the above trend. The decrease in the thermal expansion coefficient with an increase in the substitution of Ta in place of Nb can also be correlated with the B−O bond strength. This can be theoretically proven using the renormalization group method based on the ionization energy theory developed by Arulsamy.[30] The theory treats a solid as a chain of vibrating harmonic oscillators and used second-order time-independent perturbation theory with the heavier effective mass condition, as required by the electron−electron screened Coulomb potential.

dx.doi.org/10.1021/ic202383f | Inorg. Chem. 2012, 51, 2409−2419

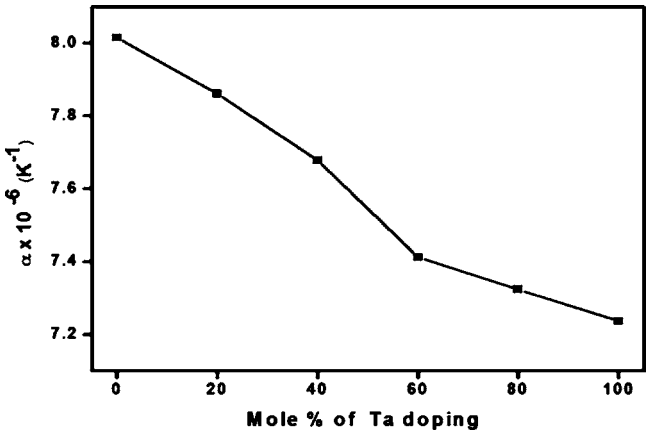

Figure 8. Variation of the lattice thermal expansion coefficient with different compositions, $CaGdZrNb_{1-x}Ta_xO_7$ (x = 0, 0.2, 0.4, 0.6, 0.8, 1). In pyrochlore-type compositions, the thermal expansion coefficient decreases with an increase in substitution of Ta. Thermal expansion of zirconate pyrochlores depends on the Madelung binding energy, and as the Madelung binding energy increases, thermal expansion decreases. The Madelung binding energy of zirconate pyrochlores depends on the 48f O x parameter, and as the x parameter decreases, the Madelung energy increases. The experimental results of our high-temperature XRD studies were in good agreement with the above trend.

Arulsamy also proved that the mathematical structure of the ionization-energy-dressed electron−electron screened Coulomb potential is exactly the same as the ionization-energy-dressed electron−phonon interaction potential. According to this theory, the square of the phonon frequency is directly proportional to the exponential of the ionization energy of the ion-bonding electrons, which is responsible for the bond. The diatomic bond energy of the Ta−O bond (799.1 ± 12.6 kJ/mol) is greater than that of the Nb−O bond (771.5 ± 25.1 kJ/mol)[31] and hence the diatomic bond strength within Ta−O is greater than that within Nb−O. The stronger bond between Ta and O implies a larger ionization energy of the bonding electrons and, therefore, the increase in the phonon frequency. Consequently, increasing the phonon frequency implies increasing the rigidity of the system, which ultimately leads to smaller thermal expansion.

3.5. Scanning Electron Microscopy (SEM) Studies. The SEM microstructures of the thermally etched polished surfaces of the sintered pellets are given in Figure 9. It is seen that all of the compounds are well-sintered with grains ranging from 1 to 8 μm in size. The average grain size for all compositions was measured from the SEM images using the linear intercept method, and the data are shown in Table 3. The micrographs further evidence the densification of the sintered pellets with less porosity. It was further observed that the $CaGdZrNbO_7$

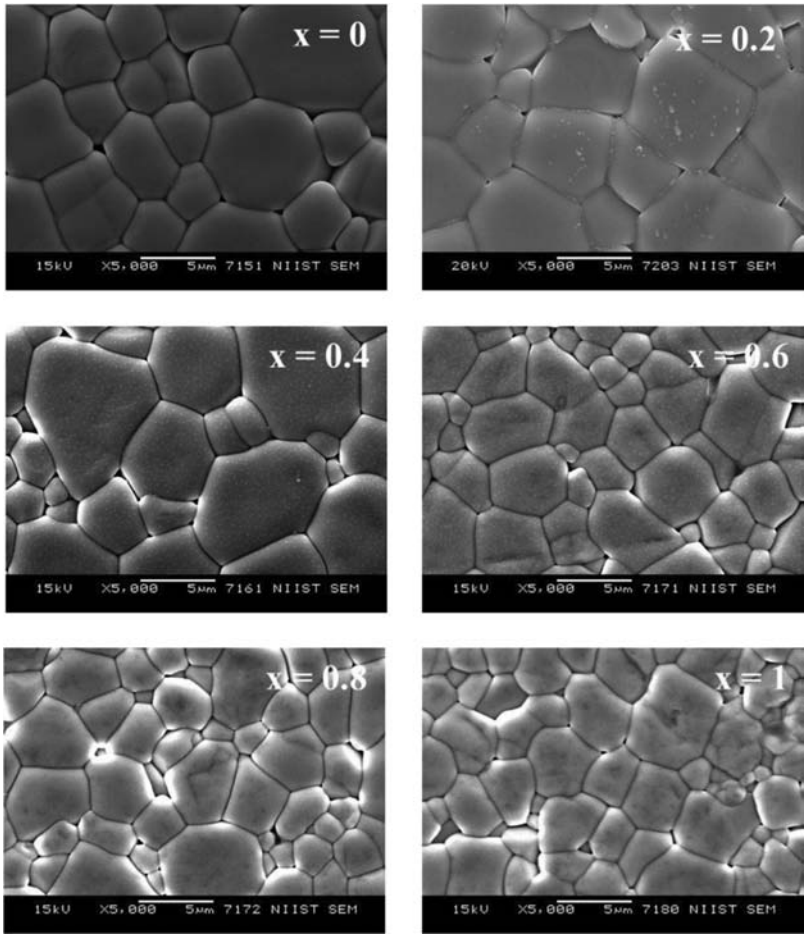

Figure 9. SEM images of polished, thermally etched surfaces of $CaGdZrNb_{1-x}Ta_xO_7$ (x = 0, 0.2, 0.4, 0.6, 0.8, 1) samples sintered at 1550 °C for 36 h. It is seen that all of the compounds are well-sintered, with grains ranging from 1 to 8 μm in size. The average grain size for all compositions was measured from the SEM images using the linear intercept method, and the data are shown in Table 3.

dx.doi.org/10.1021/ic202383f | Inorg. Chem. 2012, 51, 2409−2419

Table 3. Average Grain Size of $CaGdZrNb_{1-x}Ta_x O_7$ (x = 0, 0.2, 0.4, 0.6, 0.8, 1) Samples Calculated from SEM Images by the Linear Intercept Method

compound	average grain size (μm)
$CaGdZrNbO_7$	4.74 ± 0.76
$CaGdZrNb_{0.8}Ta_{0.2}O_7$	4.91 ± 0.70
$CaGdZrNb_{0.6}Ta_{0.4}O_7$	4.77 ± 0.79
$CaGdZrNb_{0.4}Ta_{0.6}O_7$	3.98 ± 0.33
$CaGdZrNb_{0.2}Ta_{0.8}O_7$	3.83 ± 0.30
$CaGdZrTaO_7$	3.69 ± 0.30

micrograph shows uniform grain morphology, good packing, and sharp grain boundaries.

3.6. Impedance Spectroscopic Studies. The ionic conductivity of $CaGdZrNb_{1-x}Ta_xO_7$ (x = 0, 0.2, 0.4, 0.6, 0.8, 1) samples was measured by two-probe complex impedance spectroscopy. In general, the alternating-current impedance of an ionic conductor measured by a two-probe method contains contributions from the bulk, grain boundaries, and electrode/electrolyte interface, which can be reflected in a complex plane by three successive arcs,[32] as shown in Figure 10b. The

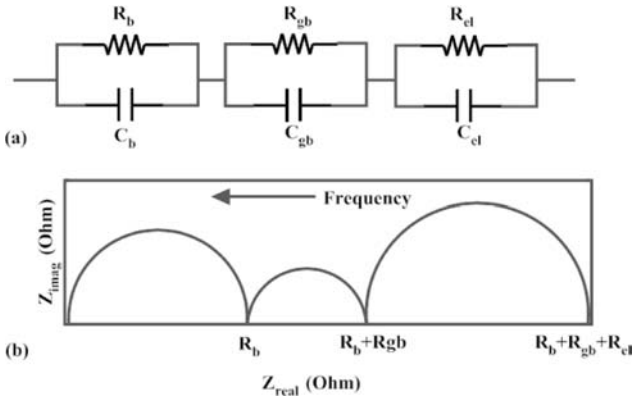

Figure 10. (a) Idealized equivalent circuit (b) and its corresponding impedance plot (a). C_b, R_b; C_{gb}, R_{gb}; and C_{el}, R_{el} represent the capacitance and resistance for the bulk, grain boundary, and electrode processes, respectively. The frequency increases from right to left across the plot. The arc at the high-frequency end of the spectrum represents the bulk resistivity; the arc at the middle of the spectrum is a consequence of the grain boundary effect; the low-frequency arc is assigned to the electrode response.

frequency increases from right to left across the plot. The arc at the high-frequency end of the spectrum represents the bulk resistivity; the arc at the middle of the spectrum is a consequence of the grain boundary effect; the low-frequency arc is assigned to the electrode response. An idealized equivalent circuit for ceramic oxides corresponding to the impedance plot is shown in Figure 10a. In a practical case, however, not all of these arcs can be observed, depending on the nature of the samples and testing conditions.[12]

Figure 11 shows the Nyquist or Cole–Cole plots obtained for different compositions during impedance measurements for three different temperatures: 400, 420, and 440 °C. It is obvious from the figure that impedance of the samples decreases with an increase in temperature, and this can be attributed to the fact that the conduction process is thermally activated. One semicircle was observed in the measured temperature range followed by a low-frequency inclined spike due to either the diffusion of ions in the electrode or electrode polarization.[33] Such a spike is characteristic of a blocking double-layer capacitance produced by the blocking of ionic charge carriers at the electrode sample interface. This also proves that charge carriers are oxide ions rather than electrons.[3] All compositions $CaGdZrNb_{1-x}Ta_xO_7$ (x = 0, 0.2, 0.4, 0.6, 0.8, 1) have negligible electronic conductivity because there are no free electrons available for conduction when the structure is stabilized with Ca (2+) and Nb/Ta (5+). If Nb/Ta gets reduced, a free electron will be created and electronic conductivity will be observed. However, even at high temperature, the structure is highly stable, with relatively low thermal expansion indicating that such Nb/Ta are still in 5+ states. The activation energy of conduction calculated from an Arrhenius plot (discussed in the latter part of the text) is in the range 0.8–0.9 eV, which is a typical value for oxide ion conduction in pyrochlores.[34,35]

The conductivity measurements of the samples were carried out from 400 to 750 °C in the frequency range 1 MHz to 10 Hz. For conductivity calculations, the resistance of the sample is read at the intersection of the semicircle with the real axis at low frequency. The conductivity (σ) is then calculated by the relation

$$\sigma = \frac{l}{RA} \tag{4}$$

where l/A is the geometrical factor, l is the thickness, and A is the area of the electrode.

The temperature dependence of the total conductivity of $CaGdZrNb_{1-x}Ta_x O_7$ (x = 0, 0.2, 0.4, 0.6, 0.8, 1) samples is shown in Figure 12. The conduction is predominantly ionic and is found to follow the Arrhenius behavior given by the equation

$$\sigma(T) = \sigma_0 \exp(-E_a/K_B T) \tag{5}$$

where σ_0 is the preexponential factor, which is a measure of the effective number of oxide mobile ions, E_a denotes the activation energy for the conduction process, K_B is the Boltzmann constant, and T is the absolute temperature. The total conductivity at 750 °C and the activation energy for the thermally activated conduction are given in Table 4. It is clear from the Arrhenius plot that the total conductivity decreases with substitution of Ta in place of Nb. Both Ta and Nb have the same ionic radius (0.64 Å) but differ in their nuclear charges and electron cloud densities. Because of the high electron cloud around Ta, the Ta–O bond is stronger compared to the Nb–O bond. Therefore, as Ta substitution increases, BO_6 octahedra will shrink and form a more rigid network of atoms. This makes diffusion of oxide ions difficult in two ways: because of reduction of the pathway for oxygen migration and because of the high activation energy required for breaking of the metal–oxygen bond. It is evident from Table 4 that the activation energy required for oxide ion conduction increases with substitution of Ta. It is also obvious that the decrease in conductivity with substitution of Ta has a small dependence on the morphological evolution of the samples with respect to doping, as seen from the SEM images. In general, as the average size of the grains decreases, the grain boundary area increases and, consequently, the conductivity decreases. The grain boundary acts as a blocking layer to ionic motion due to its change in orientation from the grain

dx.doi.org/10.1021/ic202383f | Inorg. Chem. 2012, 51, 2409–2419

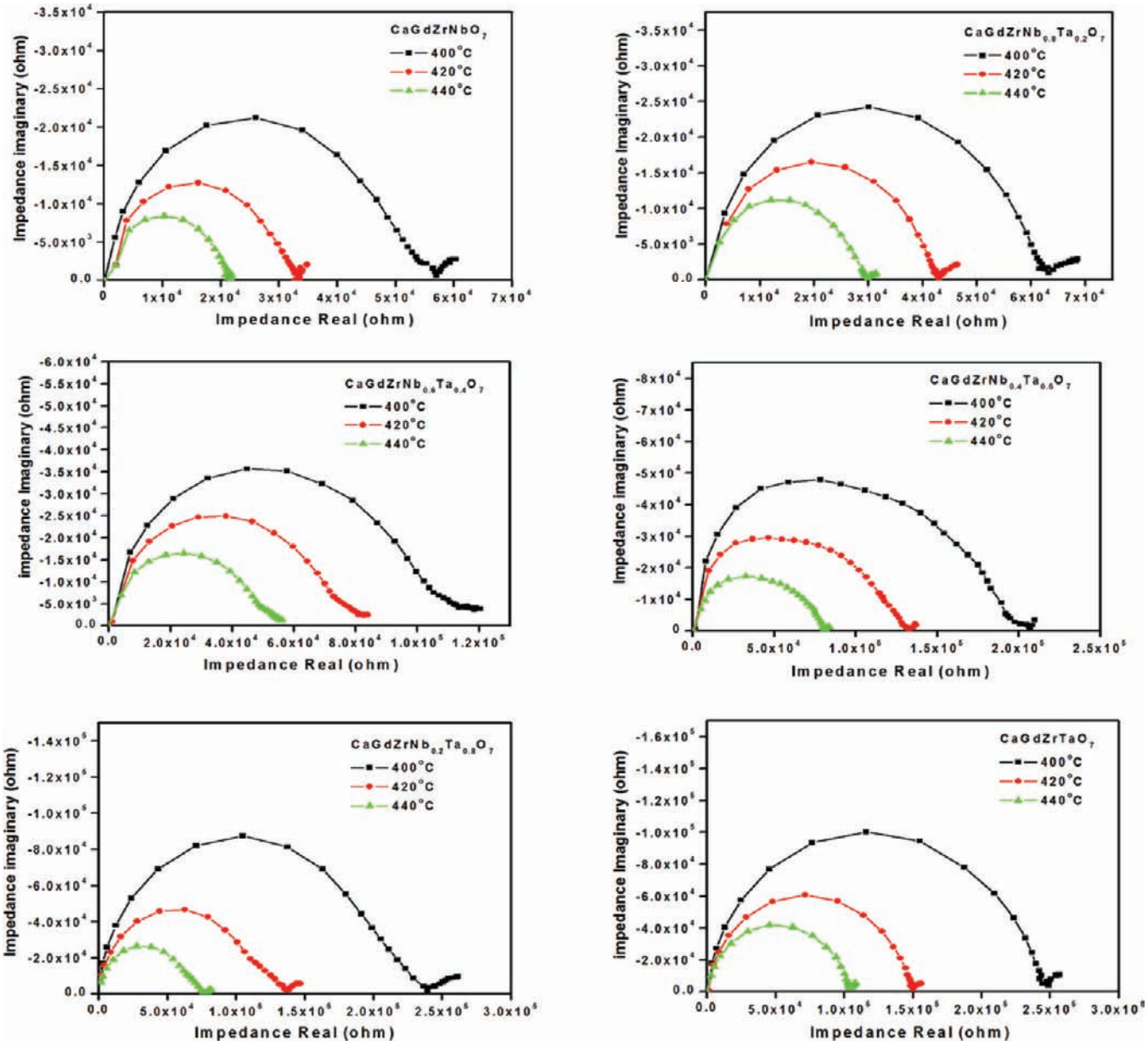

Figure 11. Cole–Cole plots of $CaGdZrNb_{1-x}Ta_xO_7$ (x = 0, 0.2, 0.4, 0.6, 0.8, 1) samples during impedance measurements for three different temperatures: 400, 420, and 440 °C. It is obvious from the figure that impedance of the samples decreases with an increase in temperature, and this can be attributed to the fact that the conduction process is thermally activated. One semicircle was observed in the measured temperature range followed by a low-frequency inclined spike due to either the diffusion of ions in the electrode or electrode polarization. Such a spike is characteristic of a blocking double-layer capacitance produced by the blocking of ionic charge carriers at the electrode sample interface. This also proves that charge carriers are oxide ions rather than electrons.

interior. This may also cause a small change in the total conductivity of the samples with respect to doping.

Oxygen ion conduction in pyrochlores, like in fluorites, proceeds via an oxygen vacancy mechanism. An ordered pyrochlore structure has an intrinsic oxygen vacancy at the 8a site, and the migration mechanism consists of jumps of 48f and 8b O ions into these vacant sites, leaving behind vacancies at their original sites.[36] In the pyrochlore lattice, contiguous pathways for oxygen ion migration are provided by jumps from a 48f site to a vacant 48f site along both ⟨100⟩ and ⟨110⟩ directions.[37,38] An alternate pathway is formed by a jump from a 48f site to a vacant 8b site followed by a jump from an 8b site to a vacant 48f site, but only along the ⟨110⟩ direction.[39] Previous computational studies have found that the 48f–48f mechanism is a more energetically favorable pathway than the 48f–8b mechanism.[40,41] Our experimental results also provide a clear indication that the 48f–48f mechanism is the dominant mechanism in the oxide ion conduction process in pyrochlore oxides because the B cation at 16c in pyrochlore is surrounded only by 48f O atoms and a change in the conductivity and activation energy with doping at the B site is observed. When the B–O bond strength increases with Ta doping, the 48f O bonded to Ta cannot easily jump to the vacancy site to initiate oxygen migration and hence the conductivity decreases.

dx.doi.org/10.1021/ic202383f | Inorg. Chem. 2012, 51, 2409–2419

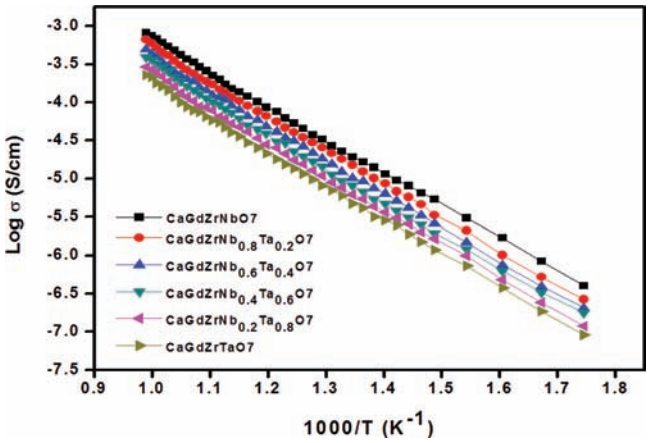

Figure 12. Arrhenius plots of $CaGdZrNb_{1-x}Ta_x O_7$ (x = 0, 0.2, 0.4, 0.6, 0.8, 1) samples. The conductivity measurements of the samples were carried out from 400 to 750 °C in the frequency range 1 MHz to 10 Hz. For conductivity calculation, the resistance of the sample is read at the intersection of the semicircle with the real axis at low frequency. The conduction is predominantly ionic and is found to follow the Arrhenius behavior given by the equation $\sigma(T) = \sigma_0 \exp(-E_a/K_BT)$, where σ_0 is the preexponential factor, which is a measure of the effective number of oxide mobile ions, E_a denotes the activation energy for the conduction process, K_B is the Boltzmann constant, and T is the absolute temperature.

Table 4. Oxide Ion Conductivity at 750 °C and Activation Energy of Conduction for $CaGdZrNb_{1-x}Ta_xO_7$ (x = 0, 0.2, 0.4, 0.6, 0.8, 1) Samples

compound	total conductivity at 750 °C (S/cm)	activation energy (eV)
$CaGdZrNbO_7$	8.13×10^{-4}	0.8628
$CaGdZrNb_{0.8}Ta_{0.2}O_7$	6.66×10^{-4}	0.8750
$CaGdZrNb_{0.6}Ta_{0.4}O_7$	4.96×10^{-4}	0.8858
$CaGdZrNb_{0.4}Ta_{0.6}O_7$	3.92×10^{-4}	0.8901
$CaGdZrNb_{0.2}Ta_{0.8}O_7$	2.89×10^{-4}	0.8963
$CaGdZrTaO_7$	2.27×10^{-4}	0.9007

4. CONCLUSIONS

$CaGdZrNb_{1-x}Ta_xO_7$ (x = 0, 0.2, 0.4, 0.6, 0.8, 1) pyrochlore oxide solid solutions were prepared by the solid-state route and sintered at 1550 °C for 36 h to optimize its density. Powder XRD and Raman spectroscopic studies were made to ensure the pyrochlore structure of the compositions. High-resolution images and SAED patterns further confirmed that samples are polycrystalline and single phase. High-temperature XRD measurement is used to calculate the thermal expansion coefficients of the samples. Thermal expansion is found to decrease with substitution of Ta in place of Nb, and this can be attributed to the high ionization energy of Ta and, consequently, to the high strength of the Ta−O bond compared to the Nb−O bond. Cole−Cole plots obtained by impedance measurements show a single arc corresponding to both grain and grain boundary contributions followed by a small spike corresponding to electrode−electrolyte double-layer capacitance. This double-layer blocking capacitance is evidence for oxide ion diffusion. The Arrhenius plot shows that Nb-rich compounds have high conductivity compared to Ta-rich compounds, and this can also be attributed to the bond strength. It can be concluded that oxide ion conduction in the pyrochlore proceeds via a 48f−48f hoping mechanism and the B−O bond strength plays an important role in determining the oxide ion conductivity of pyrochlore oxides. The above results would allow prediction of the oxide ion conductivity and lattice thermal expansion of the pyrochlore-type compounds depending on the nature of the element substituted at the B site. Doping of an element with high ionization energy increases the bond strength, and consequently both the oxide ion conductivity and thermal expansion coefficient decrease.

AUTHOR INFORMATION

Corresponding Author

*E-mail: padala_rao@yahoo.com. Tel.: + 91 471 2515311. Fax: + 91 471 2491712.

ACKNOWLEDGMENTS

A.N.R. acknowledges the Council of Scientific and Industrial Research (CSIR), Government of India, for financial support through a senior research fellowship.

REFERENCES

(1) Deepa, M.; Prabhakar Rao, P.; Sumi, S.; Radhakrishnan, A. N.; Chandran, M. R.; Koshy, P. *Mater. Chem. Phys.* **2011**, *127*, 162−169.
(2) Rao, P. P.; Nair, K. R.; Seema, K. V.; Koshy, P.; Vaidyan, V. K. *J. Mater. Sci.* **2005**, *40*, 4085−4088.
(3) Sibi, K. S.; Radhakrishnan, A. N.; Deepa, M.; Prabhakar Rao, P.; Koshy, P. *Solid State Ionics* **2009**, *180*, 1164−1172.
(4) Kharton, V. V.; Marques, F. M. B.; Atkinson, A. *Solid State Ionics* **2004**, *174*, 135−149.
(5) Hiroi, Z.; Yamaura, J. I.; Yonezawa, S.; Harima, H. *Physica C* **2007**, *460*, 20−27.
(6) Yoshimura, K.; Sakai, H.; Ohno, H.; Kambe, S.; Walstedt, R. E. *Physica B* **2003**, *329*, 1319−1320.
(7) Sickafus, K. E.; Minervini, L.; Grimes, R. W.; Valdez, J. A.; Ishimaru, M.; Li, F.; McClellan, K. J.; Hartmann, T. *Science* **2000**, *289*, 748−751.
(8) Sameera, S.; Prabhakar Rao, P.; Chandran, M. R. *J. Mater. Sci.: Mater. Electron.* **2011**, *22*, 1631−1636.
(9) Hirayama, M.; Sonoyama, N.; Yamada, A.; Kanno, R. *J. Lumin.* **2008**, *128*, 1819−1825.
(10) Stanek, C. R.; Minervini, L.; Grimes, R. W. *J. Am. Ceram. Soc.* **2002**, *85*, 2792−2798.
(11) Erickson, E. E.; Gray, D.; Taylor, K.; Macaluso, R. T.; LeTard, L. A.; Lee, G. S.; Chan, J. Y. *Mater. Res. Bull.* **2002**, *37*, 2077−2083.
(12) Kumar, M.; Raj, I. A.; Pattabiraman, R. *Mater. Chem. Phys.* **2008**, *108*, 102−108.
(13) Shimizu, Y.; Maeda, K. *Sens. Actuators, B* **1998**, *52*, 84−89.
(14) Subramanian, M. A.; Aravamudan, G.; Subba Rao, G. V. *Prog. Solid State Chem.* **1983**, *15*, 55−143.
(15) Belyaev, I. N.; Sholokhovich, M. L.; Kkhan, N. *Russ. J. Inorg. Chem.* **1978**, *23*, 1112−1114.
(16) Kutty, K. V. G.; Rajagopalan, S.; Mathews, C. K.; Varadaraju, U. V. *Mater. Res. Bull.* **1994**, *29*, 759−766.
(17) Wuensch, B. J.; Eberman, K. W.; Heremans, C.; Ku, E. M.; Onnerud, P.; Yeo, E. M. E.; Haile, S. M.; Stalick, J. K.; Jorgensen, J. D. *Solid State Ionics* **2000**, *129*, 111−133.
(18) Diaz-Guillen, J. A.; Fuentes, A. F.; Diaz-Guillen, M. R.; Almanza, J. M.; Santamaria, J.; Leon, C. *J. Power Sources* **2009**, *186*, 349−352.
(19) Takamura, H.; Tuller, H. L. *Solid State Ionics* **2000**, *134*, 67−73.
(20) Radhakrishnan, A. N.; Rao, P. P.; Linsa, K. S. M.; Deepa, M.; Koshy, P. *Dalton Trans.* **2011**, *40*, 3839−3848.
(21) Heremans, C.; Wuensch, B. J.; Stalick, J. K.; Prince, E. *J. Solid State Chem.* **1995**, *117*, 108−121.
(22) McCauley, R. A. *J. Appl. Phys.* **1980**, *51*, 290−294.
(23) Rousseau, D. L.; Bauman, R. P.; Porto, S. P. S *J. Raman Spectrosc.* **1981**, *10*, 253−290.

(24) Vandenborre, M. T.; Husson, E.; Chatry, J. P.; Michel, D. *J. Raman Spectrosc.* **1983**, *14*, 63−71.
(25) Gupta, H. C.; Brown, S. *J. Phys. Chem. Solids* **2003**, *64*, 2205−2207.
(26) Scheetz, B. E.; White, W. B. *J. Am. Ceram. Soc.* **1979**, *62*, 468−470.
(27) Michel, D.; Perez y Jorba, M.; Collongues, R. *Mater. Res. Bull.* **1974**, *9*, 1457−1468.
(28) Arenas, D. J.; Gasparov, L. V.; Qiu, W.; Nino, J. C.; Patterson, C. H.; Tanner, D. B. *Phys. Rev. B* **2010**, *82*, 214302/1−8.
(29) Shimamura, K.; Arima, T.; Idemitsu, K.; Inagaki, Y. *Int. J. Thermophys.* **2007**, *28*, 1074−1084.
(30) Arulsamy Das, A. *Ann. Phys.* **2011**, *326*, 541−565.
(31) Lide, D. R. *CRC Handbook of Chemistry and Physics: A Ready-Reference Book of Chemical and Physical Data*; CRC Press: Boca Raton, FL, 1994.
(32) Kumar, M.; Nesaraj, A.; Raj, I.; Pattabiraman, R. *Ionics* **2004**, *10*, 93−98.
(33) Abram, E. J.; Sinclair, D. C.; West, A. R. *J. Electroceram.* **2001**, *7*, 179−188.
(34) Feighery, A. J.; Irvine, J. T. S.; Zheng, C. *Ionics* **1997**, *3*, 30−35.
(35) Kramer, S. A.; Tuller, H. L. *Solid State Ionics* **1995**, *82*, 15−23.
(36) Tuller, H. L. In *Defects and disorder in crystalline and amorphous solids*; Catlow, C. R. A., Ed.; Kluwer Academic Publishers: Dordrecht, The Netherlands, 1994; p 189.
(37) van Dijk, M. P.; Burggraaf, A. J.; Cormack, A. N.; Catlow, C. R. A. *Solid State Ionics* **1985**, *17*, 159−167.
(38) Wilde, P. J.; Catlow, C. R. A. *Solid State Ionics* **1998**, *112*, 173−183.
(39) Pirzada, M.; Grimes, R. W.; Minervini, L.; Maguire, J. F.; Sickafus, K. E. *Solid State Ionics* **2001**, *140*, 201−208.
(40) van Dijk, M. P.; de Vries, K. J.; Burggraaf, A. J. *Solid State Ionics* **1983**, *9−10*, 913−919.
(41) Williford, R. E.; Weber, W. J.; Devanathan, R.; Gale, J. D. *J. Electroceram.* **1999**, *3*, 409−424.